LAWRENCE
LIVERMORE
NATIONAL
LABORATORY

LLNL-JRNL-662075

Practical error reduction and quantification in non-Gaussian shock physics measurements

M. C. Akin, J. H. Nguyen

October 6, 2014

Journal of Applied Physics

Disclaimer

This document was prepared as an account of work sponsored by an agency of the United States government. Neither the United States government nor Lawrence Livermore National Security, LLC, nor any of their employees makes any warranty, expressed or implied, or assumes any legal liability or responsibility for the accuracy, completeness, or usefulness of any information, apparatus, product, or process disclosed, or represents that its use would not infringe privately owned rights. Reference herein to any specific commercial product, process, or service by trade name, trademark, manufacturer, or otherwise does not necessarily constitute or imply its endorsement, recommendation, or favoring by the United States government or Lawrence Livermore National Security, LLC. The views and opinions of authors expressed herein do not necessarily state or reflect those of the United States government or Lawrence Livermore National Security, LLC, and shall not be used for advertising or product endorsement purposes.

Practical uncertainty reduction and quantification in shock physics measurements

M. C. Akin[1, a)] and J. H. Nguyen[1]
Lawrence Livermore National Laboratory,
Livermore, CA 94550

(Dated: 1 April 2015)

We report the development of a simple error analysis sampling method for identifying intersections and inflection points to reduce total uncertainty in experimental data. This technique was used to reduce uncertainties in sound speed measurements by 80% over conventional methods. Here, we focussed on its impact on a previously published set of Mo sound speed data and possible implications for phase transition and geophysical studies. However, this technique's application can be extended to a wide range of experimental data.

PACS numbers: 47.40.-x, 47.80.Cb, 62.50.-p, 62.50.Ef, 64.60.A-

I. INTRODUCTION

A light gas-gun experiment can produce equation of state (EOS) data, such as pressure and density (P,ρ), at extreme conditions with precision better than 0.5%.[1,2] The gas-gun based Pt EOS, for instance, has been used as a pressure scale for many high pressure experiments to date.[1,3–10] EOS data must be supplemented by phase information to understand important material behaviors, such as the melting of Fe alloys at the boundary between the solid, inner and molten, outer regions of the Earth's core.[11] Identifying a phase transition in an opaque material requires either a direct measurement such as x-ray diffraction (which presents its own challenges) or indirect measurements.

Longitudinal sound speed (C_L) measurements play a major role in constraining key phase transitions and hence constructing phase diagrams at extreme conditions.[11–17] C_L is directly related to the bulk and shear moduli. Structural changes that alter the P- or ρ-dependence of either modulus can therefore be identified through a discontinuity or change in slope of C_L. However, these changes may be subtle, on the order of a few percent, and so require high-precision, high-accuracy data. Experimental precision and accuracy depend on sample purity, data quantity, inherent data precision, and the sophistication of the data analysis methods.[11,17]

In 2004, one of us published a new measurement of Fe sound speed at Earth's core conditions.[11] The results changed the community's interpretation of the Fe phase diagram and temperature at the inner-outer core boundary. Its impact is most evident in the study of core chemistry, the mechanism through which sound waves from earthquakes travel through the core, and phase transitions at extreme conditions.[18,19] These studies point to a need for more precise C_L measurements. These experiments have pushed the limits of data measurements and are often prohibitively expensive to repeat, so the greatest gains are from improved analysis methods.

In the course of analyzing recent Mo sound speed data[17] based on a similar experimental design, we developed a Monte-Carlo based analysis technique to significantly reduce uncertainties on these data consistently to below the 1.5% level. (However, very poor signal/noise leads to larger uncertainties.) The technique reduces biases often introduced by the experimenters. It also allows one to quantitatively estimate and account for the quality of each data channel in the final error calculations, while our previous analytical technique did not.[11]

Here we present this technique as applied to the Mo C_L data[17] and data from our ongoing study of Ta C_L. We describe our new method, with details on its strengths and weaknesses as well as analysis of the method itself, which we believe is broadly applicable to any system where quantitative identification of trend deviation is desired. No *a priori* processing of raw data is required, and only basic statistics,[20] which we find advantageous in our work. A future paper will present a reanalysis of the Fe data[11] with revised uncertainties using the method discussed in this paper.

[a)] Electronic mail: akin1@llnl.gov; LLNL-JRNL-662075; This document was prepared as an account of work sponsored by an agency of the United States government. Neither the United States government nor Lawrence Livermore National Security, LLC, nor any of their employees makes any warranty, expressed or implied, or assumes any legal liability or responsibility for the accuracy, completeness, or usefulness of any information, apparatus, product, or process disclosed, or represents that its use would not infringe privately owned rights. Reference herein to any specific commercial product, process, or service by trade name, trademark, manufacturer, or otherwise does not necessarily constitute or imply its endorsement, recommendation, or favoring by the United States government or Lawrence Livermore National Security, LLC. The views and opinions of authors expressed herein do not necessarily state or reflect those of the United States government or Lawrence Livermore National Security, LLC, and shall not be used for advertising or product endorsement purposes.

FIG. 1: A 3 mm thick, 32 mm diameter molybdenum disc was counter-bored to create a stepped target. The thicknesses of these steps are flat and parallel to 2 micrometers across the pocket's entire surface. These pockets are arranged to minimize side releases and other interactions. Reprinted with permission from *Phys. Rev. B* **89** 174109 (2014).[17] Copyright American Physical Society 2014.

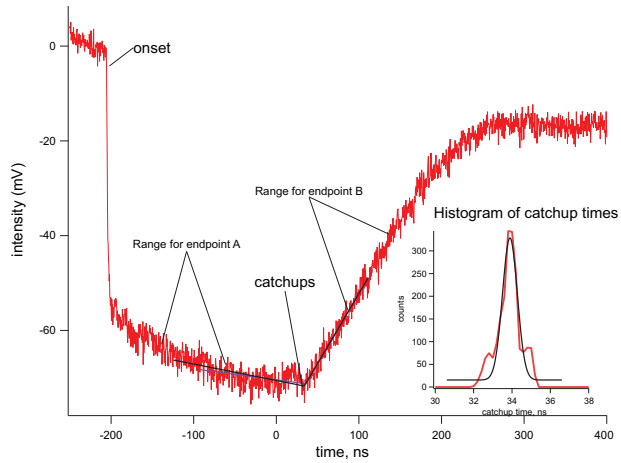

FIG. 2: Bromoform emission showing the onset, catchup, and subsequent decrease in emission. As the shock moves through the bromoform, less unshocked bromoform is available to absorb light, leading to a shallow negative slope between -200 and 30 ns. Slopes are negative because the detector is negatively biased; more negative signal indicates a greater amount of light. At ∼30 ns the release wave launched from the impactor catches up to the shock front, decreasing its strength and thus the bromoform emission; this is seen as the sharp increase in voltage beginning around 34 ns. Inset: A histogram of 2000 randomly sampled catchup times for this channel, as calculated using the algorithm described in this paper. The catchup time is determined as the mean of the Gaussian fit; the standard deviation of the fit is used as the overall uncertainty in the catchup time. Endpoints for the fits were randomly selected in the ranges shown in Fig. 2. In this case, the onset is at -205.6 ±0.2 ns and the catchup was calculated to be 33.9±0.6 ns, for an emission time of 239.5±0.7 ns. It is this 239.5 ns emission time that is plotted against the step thickness (in this case, 1.0057 mm).

II. METHODS

A. Experimental Design and Motivation

These experiments indirectly measure the speed of sound through optically opaque materials such as Fe, Mo, Ta, and Cu.[11–15,17,21] Particle velocity, U_p, is measured once the shock and sound waves pass through a sample interface (Fig. 1). The measurements are made either by recording U_p-dependent light emissions from an optical analyzer[22] (Fig. 2), or by recording U_p directly through Photon Doppler Velocimetry (PDV)[24] (Fig. 3). The analysis principles are the same for both methods, so we discuss optical analyzer data[17] from CH_3Br (Figs. 2 and 4) here. Emitted light intensity varies as $u_p^{7.6}$,[23] and so is quite sensitive. We use the less-sensitive PDV (Fig. 3) in experiments where emission is too low for fast photomultipliers, or at analyzer pressures <300 kbar.

In these experiments, impact launches shock fronts forward into the target material and backward into the impactor. When the backward-traveling shock front reaches the impactor's plastic sabot, a release wave is launched, which travels forward at the local sound speed in the compressed material. Because the material is compressed, the head of the forward-traveling release wave moves faster than the forward-traveling shock front. As a result, the release wave at first chases and then overtakes the forward-moving shock front. Prior to the release wave's arrival, the sample is in a steady state, and U_p is constant. The arrival of the release wave causes U_p and the emission to decrease, allowing overtake to be determined.

The time difference between the arrivals of the shock and release waves is the catchup time t,

$$t[x] = c - o \tag{1}$$

where o is the onset of shock breakout and c the catchup of the release wave (shown in Figs. 2-3). It is linearly dependent on the target thickness x. By measuring the catchup times for multiple thicknesses, we can extrapolate to find the ideal catchup distance D, where the shock and release waves would arrive simultaneously ($t[D] = 0$). D cannot be uniquely identified through measurement.

By determining D, the longitudinal sound speed, C_L, is calculated for symmetric impact (that is, the impactor and target are the same material) as shown:

$$C_L = \left(1 - \frac{U_p}{U_s}\right)\left(\frac{D+h}{D-h}\right)U_s \tag{2}$$

where U_s is the shock speed, and h the impactor thickness. Of these variables, D is the most difficult to determine and contributes the most to error. U_s, U_p, and h are known to better than 0.5%, and uncertainty in o is set by oscilloscope resolution (<100 ps with modern

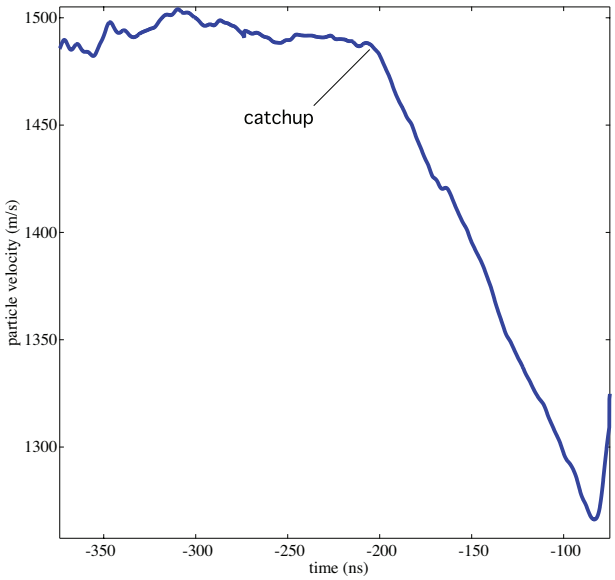

FIG. 3: Representative PDV data from ongoing Ta sound speed studies. Image is scaled to focus on catchup and release region; the sharp rise indicating breakout is not shown. The particle velocity at the sample/vacuum interface is measured and transformed according to standard PDV methods. No windows are used.

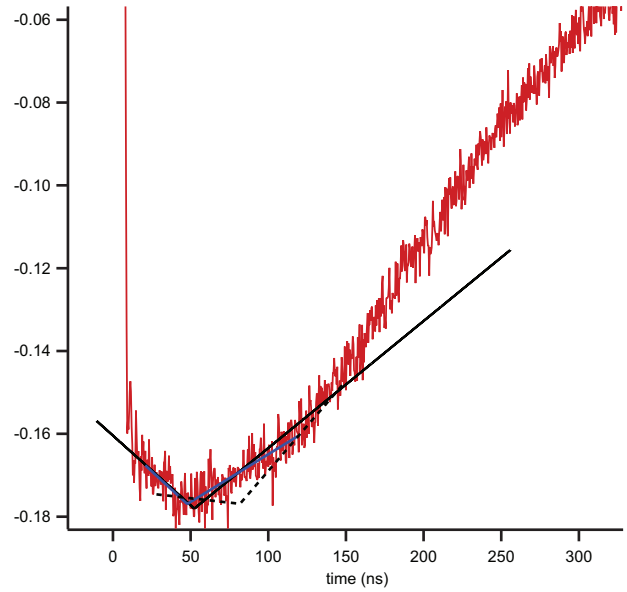

FIG. 4: Examples of different fits that can result from variations in endpoint selection. As the shock front enters the bromoform near 0 ns, the data signal drops to a large negative value. In this case, the sample is almost thick enough for the release wave to catch up to the shock front within the target. As a result there is <50 ns where the emission is constant. The "catchup" or "breakpoint," c, is the point at which emission decreases and the signal voltage becomes less negative, indicating that the release wave has arrived. In the fits shown here (dashed and solid black lines), endpoint selection varies c by 30 ns, doubling $t[x]$. With the new technique a distribution of c can be determined, which can be used to reduce the weighting of this point while still including the data in extrapolation to find D.

oscilloscopes). Like others,[22] we find the identification and uncertainty of c to drive most of the uncertainty in D and C_L.

B. Origin of error and uncertainty in c

Many factors influence the determination of c and its uncertainty Δc. These effects are exacerbated in poorer quality data or in thicker samples with a shorter t (Fig. 4). In Fig. 4, endpoint selection strongly affects catchup calculations, shifting t. Using only a single fit to calculate c, and its corresponding fit uncertainty ($\delta_i c$) as Δc, underestimates Δc, as typical $\delta_i c$ for these data are 1 ns. In the example shown in Figure 4, the difference between different fits of c were up to 30 ns. Instead, we use the standard deviation σ_c, calculated as discussed in this paper, as Δc.

Other factors include noise in the data and user-driven bias. Instrumental noise can be a few percent or more, and makes it difficult for experimenters to pinpoint c. Bias in initial fit estimates can also shift the results. Our previous method,[11] and by extension, methods used in earlier studies, did not provide a way to weight channels by data quality or $\delta_i c$, or to estimate the role of user bias. In these cases, channels with bad or multiple fits would have been excluded from the extrapolation, increasing D's overall uncertainty. Measuring the population of fits and c by varying the endpoints and the initial fit variables is one solution to all of these issues. The population's standard deviation σ_c also provides quantitative means to weight data in fitting to find D.

We chose to use random sampling instead of testing all possible combinations of endpoints for two reasons. First, sampling is much faster but yields statistically identical results. Second, proceeding through all endpoints in sequence can lead to biases. We observed small variations in calculated fits based on the initial guess for the catchup variable c. As a conceptual example, seeding a fit of the same data subset with c=240 ns vs. c=260 ns will lead to differing final fit values of 249 and 251 ns respectively. When sampling, each fit is seeded from the previous fit, and this initial bias is assumed to be averaged due to the random nature of the fitting algorithm. Results of sampled data sets where the seed values were fixed (i.e., set to 240 ns in the example above), instead of being seeded from the previous fit, are consistent with this assumption. The initial researcher-provided fit need only approximate the estimated catchup point. This reduces researcher bias in the fitting and endpoint selection.

C. Determination of D and C_L

To determine the release arrival,[11,17] we constructed a simple model function of two intersecting independent line segments. We use a standard χ^2 minimization algorithm[26] to identify the intersection point, which is c. (Fig. 2). We chose this model because it is simple, returns a single variable of interest (c), and is consistent with the previous analysis of the Fe study.

For each of the n channels per shot (6-14 channels, depending on target design), we first estimate initial fit variables, including c, for our model. We then define endpoint ranges. These are selected to avoid limiting possible solutions for c and maximize the number of possible fits. A typical range (i.e., the pool of possible endpoints) is between 150 and 400 points wide, leading to roughly 50,000 possible fits per channel. In cases where the sample thickness x_n is nearly equal to D, these ranges may be reduced.

The fitting algorithm then randomly selects endpoints and samples 1000-3000 fits to generate a histogram for c. The mean $\bar{c}$ and σ_c by are found by fitting a normal distribution to the histogram. The onset o is found and we solve

$$t[x_n] = o_n - \bar{c}_n \tag{3}$$

and

$$\Delta t[x_n] = \sqrt{(\Delta o_n^2 + \sigma_{c,n}^2)}. \tag{4}$$

Then for each shot we plot all $t[x_n]$ against x, and linearly fit, using $\Delta t[x_n]$ as the weighting, to find

$$t[x] = (a \pm \Delta a)x + (b \pm \Delta b) \tag{5}$$

We then solve for D:

$$D = \frac{-b}{a} \tag{6}$$

$$\Delta D = D\sqrt{\left(\frac{\Delta b}{b}\right)^2 + \left(\frac{\Delta a}{a}\right)^2} \tag{7}$$

We apply the results to Eqn. 2 to solve for C_L and ΔC_L.

In cases where the data include sinusoidal noise, fits of both the noisy and filtered data were performed and compared with the clean paired channel. In all cases the fits to filtered data had better agreement with the non-noisy twin and were used in the final analysis for the shot.

D. Synthetic Data

To test and validate the fitting algorithm, artificial data sets were created with known origin, and then analyzed using the same method used for experimental data. Six data forms, or test cases, were created by combining a line segment (Curve 1) with different curves, shown in Fig. 5a. While the analyzer is in a steady shocked state, the constant U_p leads to constant emission. The optical depth of the analyzer is $<< 1$, so (using Beer's Law) one can approximate the emitted light absorption by the unshocked analyzer as linearly dependent upon the thickness of the unshocked analyzer. This thickness steadily decreases in time as the shock front progresses through the analyzer, leading to an apparent linear increase in emission. This is the physical basis for selecting a linear fit in the first half of our fitting model and as Curve 1 in our synthetic data. There is, however, no reason why our method could not be applied to non-linear models.

Forms 1 and 2 are the intersection of two line segments; these differ mainly by the intersection angle. Forms 3-6 were based on the intersection of a line segment with a quadratic curve. The curvature and direction of the quadratic segments were varied to examine their effect upon the fit. The equations used to generate each of these forms are shown in Table I. Gaussian noise was added to each of these perfect (i.e., $\Sigma_N = 0$) forms at three different noise levels (Σ_N) to simulate detector and digitizer noise. Fig. 5b shows form 1 at the different noise levels. Each of the "perfect" and noisy forms was then analyzed using the fitting method.

III. RESULTS AND DISCUSSION

A. Synthetic Data: Algorithm sensitivity to data form and noise levels

Results of the analysis using synthetic data are shown in Table II. In cases 1 and 2 the noise-free data returned a single value for the breakpoint (i.e., the standard deviation σ_c=0), which matched the calculated "perfect" value, as expected. The uncertainty of a single fit, $\delta_i c$, for each fit was small (10^{-8} units). The difference between σ_c and $\delta_i c$ is due to a combination of floating point precision, round off errors in calculations, and the minimization algorithm of IgorPro,[27,28] which stops after a specified minimum change in χ^2 or a set number of iterations.

As the noise levels increase, the mean $\bar{c}$ deviates from the perfect c, and the calculated error and uncertainty increase. Regardless of the noise level, σ_c is smaller than the typical $\delta_i c$, and captures the true c within $2\sigma_c$ (Figs. 6a and 6b and Table II). As shown in Figs. 6a and 6b, the calculated fits cluster into a distribution that can be reasonably fit by a Gaussian. Note that in both Fig. 6a and Fig. 6b, the perfect case has a peak value of 10,000, which was the number of fits made; this has been truncated in the figures to better show the distributions of the noisier cases.

When some curvature is added to the data, as was done in Cases 3-6, the fits became poorer in quality, and the mean $\bar{c}$ deviated further from the "perfect" c. In

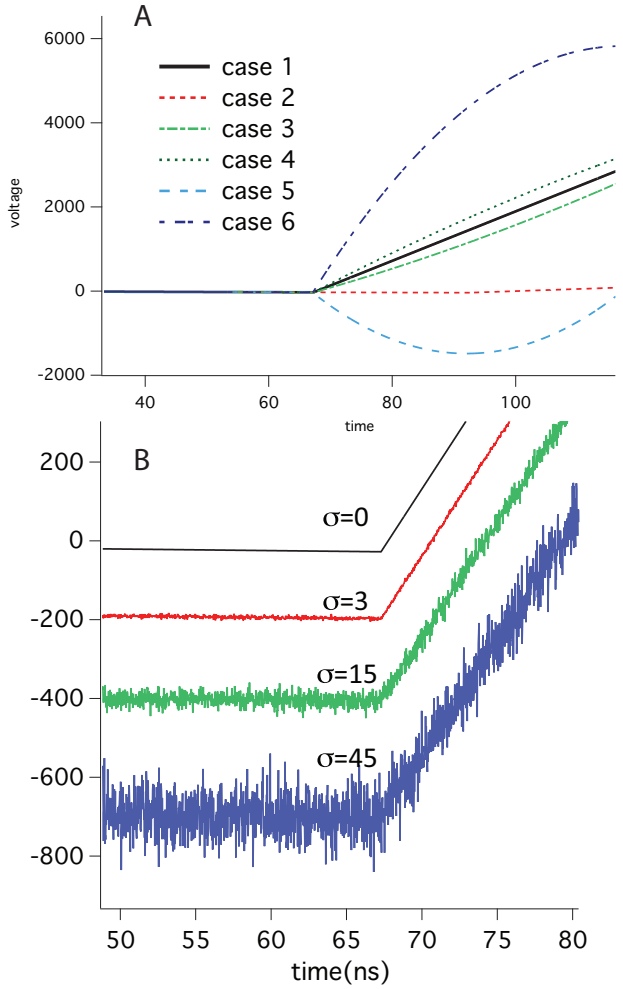

FIG. 5: Plots of the curves used to generate synthetic data. Subfig. A shows the non-noisy "perfect" curves, with $\sigma_N = 0$. In all cases, curve 1 is identical. Subfig. B shows the effects of the different noise levels used to generate noisy synthetic data for Case 1. The different noise levels have been offset vertically for clarity.

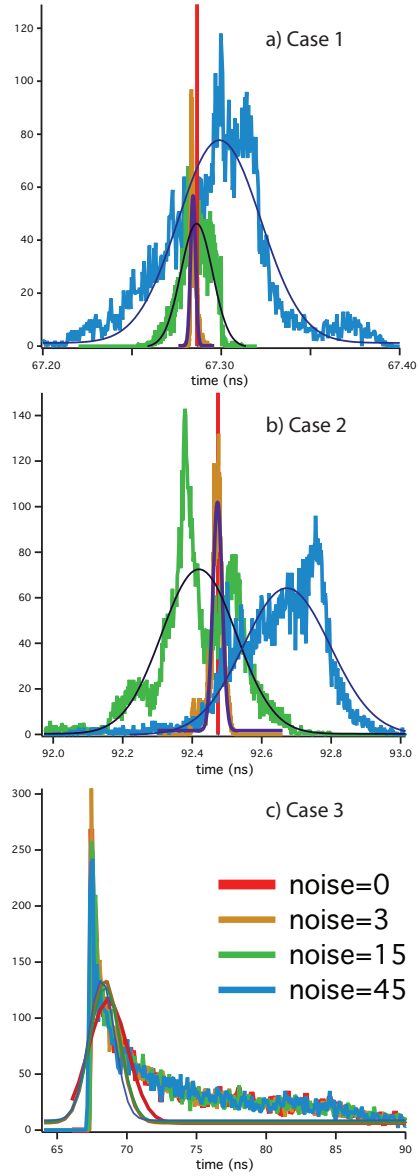

FIG. 6: The distribution of calculated breakpoints c for a.) Case 1 b.) Case 2 and c.) Case 3 at each noise level. Legend is the same for each subfigure. Increased noise leads to a broader distribution and increased uncertainty (σ_c). Cases 1 and 2: Note that the zero-noise distribution has only a single value, which peaks at a count of 10000, the sample size. It has been truncated in these graphs to improve visibility of the other histograms. Case 3: The histograms for Cases 4-6 have similar structures. This distribution shows a sharp edge, and is poorly fit by a Gaussian distribution. Increased noise in the data appears to have little effect on the resulting distribution other than to decrease the peak value and lead to a more box-like distribution. These non-Gaussian distributions are unusual in the calculated breakpoints of real data.

forms 5 and 6, including all data beyond the inflection points led to extremely poor distributions. In these cases, the range of endpoints was truncated to exclude points occurring after the inflection point of the second curve. However, the true c remained within $2\sigma_c$ of the mean $\bar{c}$ for each distribution, even though a linear model was used to analyze data with known curvature.

For these higher curvature cases, the typical uncertainty found in a single fit underestimates the error associated with the data. As can be seen in Fig. 6c, the distribution of calculated breakpoints is not Gaussian, and shows both a sharp edge and a long tail. If a boxcar distribution is assumed instead of a Gaussian, the underestimation of the uncertainty worsens. These distributions are very unusual in cases of real data, implying curvature is minimal, and consistent with our observations that most of the data channels resemble Figure 2.

Future work on applications to non-linear data is discussed later in the text.

B. Model Performance with Experimental Data

Sample histograms of the fitted catchup times, c, from our recent Mo study,[17] are shown in Figs. 7a-7c, as well as the inset of Fig. 2. As can be seen, a variety of distributions result. Most histograms are fit well by a Gaussian distribution similar to those shown in Fig. 2, inset, and Fig. 7a. In these cases, the mean of single Gaussian distribution $\bar{c}$ was used to determine the fit value, with the standard deviation as the uncertainty σ_c.

Histograms of c were weighted by the uncertainty of each individual fit ($\delta_i c$), which we used as a goodness-of-fit estimator. We found that this made little to no difference in $\bar{c}$ and σ_c when compared to the first method, which was to equally weight each fitted value for c. Therefore we discarded such weighting as an unnecessary extra step and used equal weighting instead. σ_c is almost always larger than $\delta_i c$, which, based on the performance of the synthetic data, suggests some curvature is present in the experimental data. However, a Gaussian distribution is sufficient in most cases, indicating the curvature is small enough to use our model. In the cases where σ_c was smaller than $\delta_i c$, we argue by the rule of large numbers that the narrow distribution is a better indicator of the true catchup time c.

Fig. 7a shows a special subset of experimental data. One in twelve channels suffered from 13.1 MHz sinusoidal noise, which originated in the oscilloscope. For each of these channels, a sine wave was fit to the noise, which is present prior to the shock breakout, and used to filter the data. The sampling algorithm would then be done on both the unfiltered and filtered data to calculate $\bar{c}$ and σ_c. Each step had two probes, allowing the filtered and unfiltered data to be compared to the result of the unaffected "non-noisy" paired probe. The result of filtering, on all shots, was improved agreement with the non-noisy twin channel from the same step. This led to improved uncertainty in D, which was used in the calculation of C_L.

Not all histograms result in normal distributions, as shown in Figs. 7b and 7c. The differences in these distributions arise from the data. In the case of bimodal distributions like Fig. 7b, the choice of one peak over another affects the final calculation of D. These distributions may arise if there is a small slope change in the data, but are generally not obvious in their origin. There is no clear way to choose one value over another. We chose instead a single broad distribution to overestimate σ_c, and reduce this channel's weighting in the calculation of D, rather than exclude the point. We also considered the box-like distribution of this histogram, which used one-third the width of the box as the estimate for σ_c. However, we prefer the most conservative uncertainty estimate, which in this case was the wide Gaussian distribution.

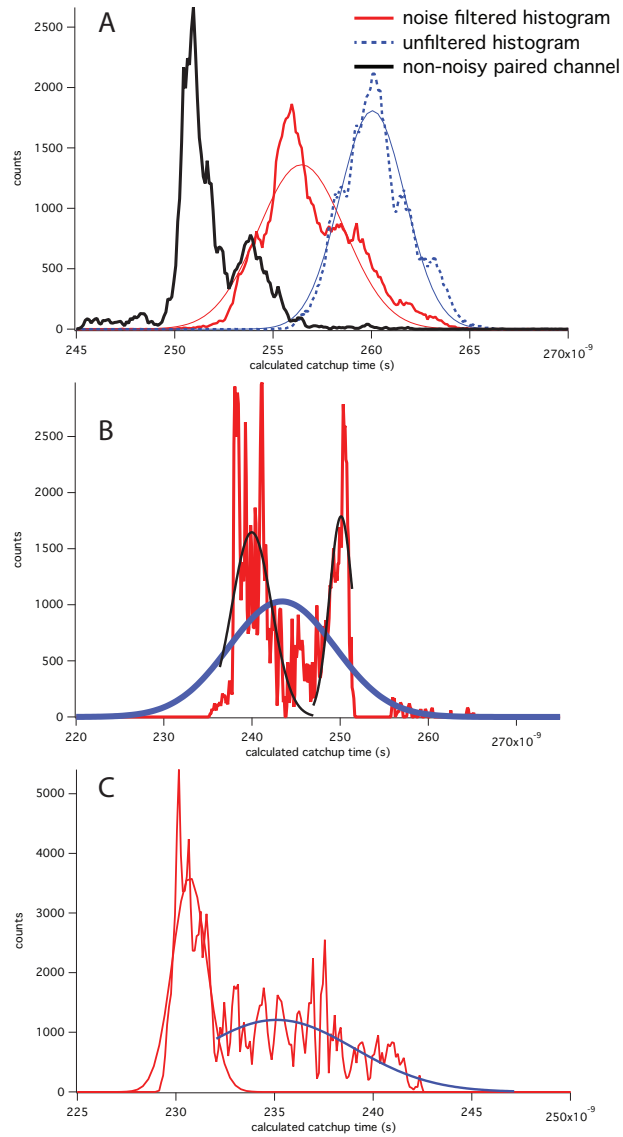

FIG. 7: Combined comprehensive fits for different channels from Mo sound speed studies, showing variations in distributions. Subfig. A: Distributions of fits to data affected by 13.1 MHz sinusoidal noise before (dashed blue) and after (solid red) filtering. Filtering improved agreement with the non-noisy twin signal (solid black) collected at the same spot. This improved agreement reduced the uncertainty in the catchup distance D, despite typically larger σ in filtered channels. Subfig. B: Endpoint ranges were chosen such that catchup c could fall between 200 and 291 ns. Fitted values fell between 237 and 252 ns. The multi-modal structure arises from the data. In the final calculation, a single Gaussian fit (heavy, blue) which spans the full range of the histogram was used to calculate the uncertainties; this method overestimates the uncertainty due to the fit. Subfig. C: Endpoint ranges were chosen such that $196 < c < 271$ ns. The fitted values fell between 229 and 243 ns. For simplicity and consistency a broad Gaussian (blue) which overestimates the uncertainty was chosen for the fit. An asymmetric fit can be extracted but yields a D that is statistically identical to that for the broadened Gaussian fit.

A similar approach was taken for the data in Fig. 7c, which can be treated as an asymmetric Gaussian distribution, with $\bar{c}$ ∼232 ns, a lower σ_c of ∼.8 ns, and an upper σ_c of 5 ns. Doing so did not significantly change the extrapolated D compared to using a single broad Gaussian distribution with larger σ_c, while requiring a good deal more effort, so in these cases we use the single larger σ_c. If such distributions were more common, it would be worthwhile to develop an alternate fitting model.

This estimation of σ_c provides a means to weight the extrapolation, resulting in D with smaller propagated uncertainties than determined by previous methods. As a result, the typical 1σ uncertainty in the Mo C_L is 0.5%. By comparison, analysis of the same data using the previous algorithm had typical uncertainties of ∼2% and a maximum uncertainty of 7%. This method, flawed as it is and designed to overestimate the uncertainties, reduces those uncertainties by roughly 80%, a significant improvement.

We tested and rejected several alternate algorithms. One alternate method of choosing the endpoint range, which looked for inflection points in the χ^2 value with time, was found to artificially narrow the possible range of catchup points, reducing estimated σ_c. We also used a one-sided linear fit instead of our two-segment model, and looked for the point where the signal appeared to deviate from that fit. This method led to consistent biases associated with the data noise level and the fitted region, but was useful estimating the data range that must be included in every fit.

Future work could further improve the results by switching to a linear-quadratic, quadratic-linear, or quadratic-quadratic model. Trend analysis could also be improved through estimation of noise variance in the data prior to shock breakout, and calculation of models and fitting parameters to minimize observed variation (maximize trend stationarity) following breakout. This method would likely yield a set of suitable functions, which would not need to be constrained to linear-linear or linear-quadratic models, from which a range of breakpoints would be determined. However, this would require additional assumptions regarding noise behavior and greater complexity.

ACKNOWLEDGMENTS

We thank our collaborators on the sound speed studies, Paul Asimow, Oleg Fat'yanov, Ricky Chau, W. Pat Ambrose, and Neil Holmes, for useful discussions that refined this method, and our reviewer and editor, for their thoughtful comments, which improved this paper. We also thank Papo Gelle, Mike Long, Mike Burns, Toni Bulai, Russ Oliver, Bob Nafzinger, Paul Benevento, Sam Weaver, Neal Hinsey, Mark Owens, and Cory McLean for their dedicated effort. This work performed under the auspices of the U.S. Department of Energy by Lawrence Livermore National Laboratory under Contract DE-AC52-07NA27344..

[1] N. C. Holmes, J. A. Moriarty, G. R. Gathers, and W. J. Nellis, *J. Appl. Phys.* **66**, 2962 (1989).
[2] A. C. Mitchell and W. J. Nellis, *J. Appl. Phys.* **52**, 3363 (1981).
[3] H. K. Mao, Y. Wu, L. C. Chen, J. F. Shu, and A. P. Jephcoat, *J. Geo. Res.-Solid Earth and Planets* **95**, 21737, (1990).
[4] Y. K. Vohra and A. L. Ruoff, *Phys. Rev. B* **42**,8651 (1990).
[5] A. Kavner and T. S. Duffy, *J. Appl. Phys.* **89**, 1907 (2001).
[6] Y. Akahama, H. Kawamura, and A. K. Singh, *J. Appl. Phys.* **92**,5892 (2002).
[7] L. S. Dubrovinsky, S. K. Saxena, F. Tutti, S. Rekhi, and T. LeBehan, *Phys. Rev. Lett.* **84**, 1720 (2000).
[8] B. K. Godwal, T. C. Kaushik, and S. K. Sikka, *Laser and Particle Beams* **15** 353, (1997).
[9] H. Shu, S. Fu, X. Huang, J. Wu, H. Zhou, and J. Ye, *Meas. Sci. Technol.* **23** 015203, (2012).
[10] K. Miyanishi, N. Ozaki, E. Brambrink, H. G. Wei, A. Benuzzi-Mounaix, A. Ravasio, A. Diziere, T. Vinci, M. Koenig and R. Kodama, *Int. Conf. High Pressure Science and Technology, Joint AIRAPT-22 and HPCJ-50*, 215 (2010).
[11] J. H. Nguyen and N. C. Holmes, *Nature* **427**, 339, (2004).
[12] R. S. Hixson, D. A. Boness, J. W. Shaner, and J. A. Moriarty, *Phys. Rev. Lett.* **62** (6), 637 (1989).
[13] R. S. Hixson and J. N. Fritz, *J. Appl. Phys.* **71** 1721 (1992).
[14] J. M. Brown and J. W. Shaner, in *Shock Waves in Condensed Matter – 1983*, edited by J. R. Asay, R. A. Graham, and G. K. Straub (Elsevier, New York, 1984), p. 91.
[15] J. M. Brown and R. G. McQueen, *Geophys. Res. Lett.* **7** (7), 533 (1980).
[16] T. S. Duffy and T. J. Ahrens, *J. Geophys. Res.* **97** 4503 (1992).
[17] J. H. Nguyen, M. C. Akin, R. Chau, D. E. Fratanduono, W. P. Ambrose, O. V. Fat'yanov, P. D. Asimow, and N. C. Holmes, *Phys. Rev. B* **89**, 174109 (2014)
[18] D. Alfè, *Phys. Rev. B* **79**, 060101 (2009).
[19] Z. Mao, J. F. Lin, J. Liu, A. Alatas, L. Gao, J. Zhao, and H. K. Mao, *Proc. Natl. Acad. Sci. U.S.A.* **109**, 1023910244 (2012).
[20] P. R. Bevington, *Data Reduction and Error Analysis for the Physical Sciences*, McGraw-Hill, New York (1969).
[21] P. A. Rigg, R. J. Scharff, and R. S. Hixson, *18th APS-SCCM and 24th AIRAPT; J. Physics: Conference Series* **500** 032018 (2014).
[22] R. G. McQueen, J. W. Hopson, and J. N. Fritz, *Rev. Sci. Instrum.* **53** 245, (1982).
[23] R. G. McQueen and D. G. Isaak, in *Shock Compression of Condensed Matter – 1989*, edited by S. C. Schmidt, J. N. Johnson and L. W. Davison, (North-Holland, Amsterdam, Netherlands, 1990) p.125.
[24] O. T. Strand, D. R. Goosman, C. Martinez, T. L. Whitworth and W. W. Kuhlow, *Rev. Sci. Instrum.* **77**, 083108 (2006).
[25] D. Yaziv, Z. Rosenberg and Y. Parton, *J. Phys. D:Appl. Phys.* **13** 2243 (1980).
[26] IgorPro, Wavemetrics.com.
[27] J. Weeks, WaveMetrics, personal communication, 25 November 2014.
[28] W. H. Press, S. A. Teukolsky, W. T. Vetterling, and B. P. Flannery, *Numerical Recipes in C: The Art of Scientific Computing, 2nd Ed.*, Cambridge: Cambridge University Press, (1990).

TABLE I: Forms chosen to generate artificial data for testing. Curve 1 was the same in all cases, $y = -4t - .64$, while Curve 2 was varied as listed in the table. Three fixed noise levels ($\Sigma_N = 3$, 15, or 45, or cases b, c, and d, respectively) were applied to the analytically calculated ($\Sigma_N = 0$, or case a) data to examine the effect of noise on the analysis. The "perfect breakpoint" given in the table below is the intersection of the two curves; results of each case should be compared to this number. The intersections are chosen to be approximately the same (but *not* tuned to be identical) in cases 3-6.

	noise level				curve 1: $y = -4t - .64$	c, perfect
Case	$\Sigma_N = 0$	$\Sigma_N = 3$	$\Sigma_N = 15$	$\Sigma_N = 45$	curve 2:	breakpoint
1	1a	1b	1c	1d	$y = 58.8t - 3984$	67.2865
2	2a	2b	2c	2d	$y = 5t - 500$	92.4741
3	3a	3b	3c	3d	$y = .233x^2 + 10.026x - 1760$	67.3566
4	4a	4b	4c	4d	$y = -.233x^2 + 107.57x - 6208$	67.2518
5	5a	5b	5c	5d	$y = 2.33x^2 - 428.94x + 18258$	67.0502
6	6a	6b	6c	6d	$y = -2.33x^2 + 546.54x - 26226$	67.1696

TABLE II: Results of analysis of artificial data. The perfect breakpoint c is calculated from the intersection of the curves listed in Table I. The curves of Table I were fitted using our sampling algorithm, with the results plotted as histograms. The calculated breakpoints shown in this table are calculated from the mean of the Gaussian fit of the histogram of fits at each of the different noise levels. The calculated uncertainties of the breakpoint are the standard deviation of the fit to the histogram of calculated breakpoints. The uncertainty of each fit was also tabulated, and the most common uncertainty is given in the table below.

	c, perfect	$\bar{c}$, calculated breakpoints				calc. std. dev. σ_c				typical single fit uncertainty $\delta_i c$			
Case	breakpoint	$\Sigma_N = 0$	$\Sigma_N = 3$	$\Sigma_N = 15$	$\Sigma_N = 45$	$\Sigma_N = 0$	$\Sigma_N = 3$	$\Sigma_N = 15$	$\Sigma_N = 45$	$\Sigma_N = 0$	$\Sigma_N = 3$	$\Sigma_N = 15$	$\Sigma_N = 45$
1	67.2865	67.2865	67.284	67.286	67.299	1.91E-10	1.96E-3	0.0124	0.0328	4.13E-08	2.9E-3	0.0146	0.0434
2	92.4741	92.4741	92.473	92.419	92.672	1.49E-11	0.0190	0.152	0.177	9.38E-09	0.0313	0.153	0.466
3	67.3566	68.645	68.392	68.425	68.184	1.997	1.488	1.525	1.325	0.0675	0.0514	0.0719	0.0828
4	67.2518	66.735	66.375	66.537	66.624	0.690	1.36	1.07	1.03	0.0119	0.0051	0.0181	0.0541
5	67.0502	66.7177	66.737	66.910	66.868	0.348	0.342	0.158	0.120	7.71E-3	4.83E-3	0.0195	0.0555
6	67.1696	66.9619	66.997	67.026	67.147	0.297	0.237	0.183	0.0122	6.37E-3	2.66E-3	8.98E-3	0.0238